International Forum on Aeroelasticity and Structural Dynamics
IFASD 2026
17-21 June 2026, Goettingen, Germany

ADAPTIVE CONTROL LAW FOR ACTIVE FLUTTER SUPPRESSION IN PRESENCE OF ACTUATION FAILURE

Elena Roncolini[1], Giovanni M. Carossa[1], Francesco Toffol[1], Sergio Ricci[1]

[1]Politecnico di Milano
Via Privata Giuseppe La Masa, 34/B12, 20156, Milan, Italy
elena.roncolini@polimi.it
giovannimarco.carossa@polimi.it
francesco.toffol@polimi.it
sergio.ricci@polimi.it

Keywords: Active Flutter Suppression, actuator fault, control allocation

Abstract: An aero-servo-elastic state-space model of a semi-wing equipped with two control surfaces experiencing flutter is studied. The adopted control strategy is divided in two blocks: classical Linear Quadratic Gaussian (LQG) with Loop Transfer Recovery (LTR) corrections for the Active Flutter Suppression (AFS), and an allocator block to re-distribute the control workload in case of actuation stuck. The analyses show that the presence of the allocator, even though not mandatory to keep stability, significantly reduces the response time decays along with control energy waste.

1 INTRODUCTION

To meet the sustainability requirements set by climate change, research and industry agree that future aircrafts will be equipped with high aspect ratio wings. Among the challenges posed by the increase in aspect ratio, higher structural flexibility is involved, and adverse aeroelastic phenomena become more likely to occur.
Within the European Union, the Clean Aviation Joint Undertaking was created to research new aviation technologies compliant with the climate crisis. In this context, the *Hybrid- Electric Regional Architecture* (HERA) project started in January 2023. The aim is to study a new regional aircraft configuration capable of reducing the emissions both flight related and technology-based [1]. As partner of the project, POLIMI was asked to create an Active Flutter Suppression (AFS) demonstrator consisting of a high aspect ratio wing equipped with two control surfaces (tab as outer, aileron as inner), here referenced to as WTT4. The demonstrator will be tested inside POLIMI large wind tunnel during summer 2026.
AFS systems are currently non-certifiable for flying aircrafts, due to lack of reliability on real operational conditions [2]. Nontheless, they have been research topic for many years, and even if certification rules do not explicitly comply with the presence of such systems, there are literature precedents where similar concepts have been implemented on commercial aircrafts [3]. To enhance the reliability of AFS, worst case scenarios along the control chain must be carefully addressed. In the present work, exploiting the presence of two control surfaces on WTT4 model, actuation fault has been simulated and dealt with by means of a control allocator to redistribute the workload on the safe actuator. The effects on system stability and control performances have been assessed.

In the following, the WTT4 state-space numerical model will be described along with flutter analysis results. Then, a first-block control strategy consisting in a Linear Quadratic Gaussian

with Loop Transfer Recovery (LQG/LTR) will be illustrated. Fault will then be introduced by means of actuator stuck. A second-block will be added to the control strategy, introducing, after the nominal LQG/LTR, an allocator block with adaptive capacity, responsible of redistributing the control workload towards the safe actuator. Finally, conclusions will be derived along with future developments.

2 WTT4 MODEL

To generate the numerical model, POLIMI in-house tool NeoCASS [4–6] has been used. The structure has been modeled through FEM by means of beam elements, whilst DLM has been exploited for aerodynamics. Since the demonstrator required in the HERA project consists of a half wing, the left semi-wing has been retained and its stiffness and inertia properties have been scaled through an iso-frequency law with a 1:6 scale factor, following the procedure reported in Appendix B of [7]. Starting from the resulting properties, a detailed CAD has been generated and manufactured. The assembled experimental model is shown in Fig. 1.

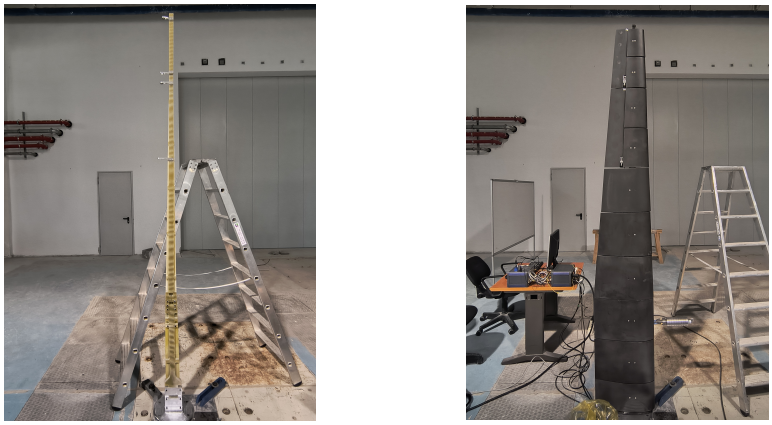


Figure 1: WTT4 experimental model: spar (left), assembly (right).

As anticipated, the model will be tested for flutter inside POLIMI large wind tunnel. A flutter safety system has been designed such that a sliding mass, mounted on a linear pneaumatic actuator placed at the wing tip, is pushed from the rear to the forward position when the wing experiences accelerations over a prescribed threshold. The approach is the same described in [8].

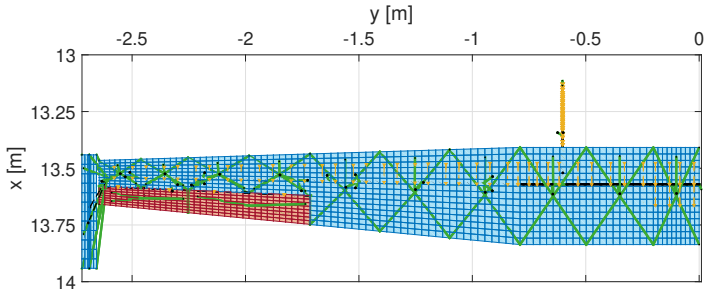


Figure 2: WTT4 NeoCASS model.

The complete WTT4 numerical model, including the tip pod, is shown in Fig. 2. Table 1 presents the first five modal frequencies and modes, whilst Fig. 3 shows first and third modal shapes, being the coalescing modes leading to flutter.

Flutter is expected at $V_{fl} = 42$ [m/s], as visible from Fig. 4. These results have been obtained introducing a 1% of structural damping.

Table 1: WTT4 modal analysis results

Mode	Description	f, Hz
1	First bending	1.59
2	First inplane	3.09
3	Second bending and first torsion	5.12
4	Second torsion	8.57
5	Third bending and torsion	9.00

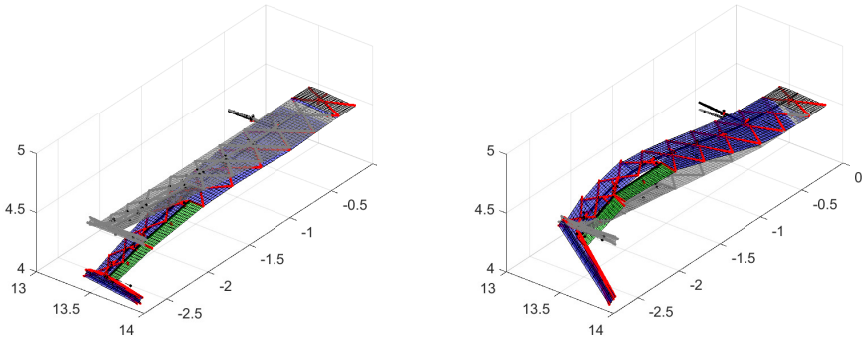


Figure 3: WTT4 first (left) and third (right) modal shapes.

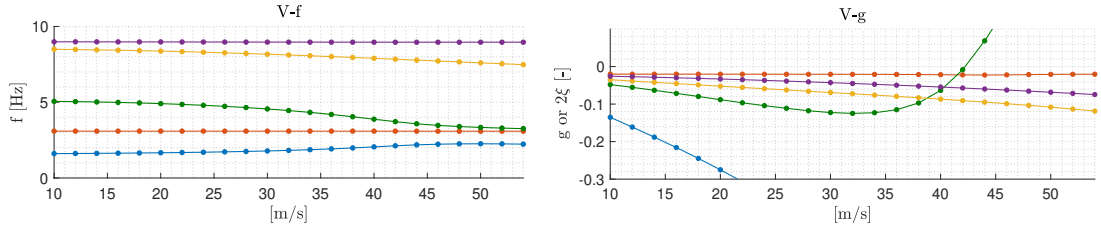


Figure 4: WTT4 V-f (left) and V-g (right) plots, first five modes.

2.1 State-space model

The Aero-Servo-Elastic (ASE) state-space model has been created interfacing structural dynamics, aerodynamics and actuators dynamics.

2.1.1 Structural dynamics

The system's equations of motion have been projected onto modal basis retaining the first 22 eigenmodes, with the first two being the control surfaces rigid modes. The resulting equations are presented in Laplace domain in 1.

$$(\mathbf{M}s^2 + \mathbf{C}s + \mathbf{K})\mathbf{q} = q_\infty \mathbf{H}_{am}(k)\mathbf{q} + \mathbf{Q} \tag{1}$$

$\mathbf{M}$, $\mathbf{C}$, $\mathbf{K}$ are the generalized mass, damping and stiffness matrices, whilst $\mathbf{H}_{am}(k)$ is the unsteady generalized aerodynamic force matrix, expressed as function of the reduced frequency k. $\mathbf{Q}$ is a generalized external force, later connected to the actuators subsystem. The vector $\mathbf{q}$ represents the 22 generalized modal coordinates. In time domain, the structural subsystem reads:

$$\begin{cases} \dot{\mathbf{q}} = \dot{\mathbf{q}} \\ \mathbf{M}\ddot{\mathbf{q}} = -\mathbf{C}\dot{\mathbf{q}} - (\mathbf{K} - q_\infty \mathbf{H}_{am}(k))\mathbf{q} + \mathbf{Q} \end{cases} \tag{2}$$

2.1.2 Aerodynamics

The generalized aerodynamic force matrix has been transformed from frequency to time domain as:

$$\mathbf{H}_{am}(p) \simeq \mathbf{D}_a^0 + p\mathbf{D}_a^1 + p^2\mathbf{D}_a^2 + \mathbf{C}_a(p\mathbf{I} - \mathbf{A}_a)^{-1}(\mathbf{B}_a^0 + p\mathbf{B}_a^1 + p^2\mathbf{B}_a^2) \tag{3}$$

with $p = \sigma + jk$ the normalized Laplace variable. Matrices $\mathbf{A}_a$, $\mathbf{B}_a^i$, $\mathbf{C}_a$ and $\mathbf{D}_a^i$ have been calculated through the rational matrix approximation algorithm proposed in [9]. In time domain, the aerodynamics subsystem becomes:

$$\begin{cases} t_a\dot{\mathbf{x}}_a = \mathbf{A}_a\mathbf{x}_a + \mathbf{B}_a^0\mathbf{q} + t_a\mathbf{B}_a^1\dot{\mathbf{q}} + t_a^2\mathbf{B}_a^2\ddot{\mathbf{q}} \\ \mathbf{Q}_a = \mathbf{C}_a\mathbf{x}_a + \mathbf{D}_a^0\mathbf{q} + t_a\mathbf{D}_a^1\dot{\mathbf{q}} + t_a^2\mathbf{D}_a^2\ddot{\mathbf{q}} \end{cases} \tag{4}$$

where $\mathbf{Q}_a = \mathbf{H}_{am}(k)\mathbf{q}$ is the generalized aerodynamic force vector, normalized by the dynamic pressure, whilst $\mathbf{x}_a$ is the vector of the 18 aerodynamic states considered in the present work.

2.1.3 Actuators dynamics

In the physical model, each control surface is actuated through a miniaturized electric motor from Harmonic Drive. Each actuator produces a hinge moment on the aeroelastic plant here considered in the form:

$$\begin{aligned} m_h &= K_{act}(H(s)u_{cmd} - \delta) \\ &= K_{act}(u_{cmd_{filt}} - \delta) \end{aligned} \tag{5}$$

where u_{cmd} is the rotation generated by the active control and $u_{cmd_{filt}}$ is the same rotation filtered by the actuator dynamics. δ is the actual control surface rotation, received as feedback from the aeroelastic plant: $\delta = \mathbf{U}_\delta\mathbf{q}$, with $\mathbf{U}_\delta$ the vector of the modal base correspondent to the control surface rotational degree of freedom. As anticipated, each actuator is connected to structural dynamics subsystem through the generalized external force vector $\mathbf{Q}$: $m_h = \mathbf{U}_\delta\mathbf{Q}$.
K_{act} has been defined supposing a modal frequency for the aileron only mode of $f = 25$ [Hz]. Knowing the aileron's inertia around the shaft axis, $K_{act} \simeq 103$ [Nm] has been obtained. Even though the tab is smaller than the aileron, the same stiffness has been considered for both the control surfaces, to model the same connection between each control surface and the wing spar. The actuators dynamics, represented by $H(s)$ of Eq. 5, has been modeled as a second order system with damping factor $\xi = 0.7$ and natural frequency $f_0 = 10$ [Hz], accordingly to the actuator's bandwidth that will be employed in wind tunnel testing for both control surfaces. In time domain, the actuator subsystem reads:

$$\begin{cases} \dot{x}_{act} = \dot{x}_{act} \\ \ddot{x}_{act} = -\omega_0^2 x_{act} - 2\xi\omega_0\dot{x}_{act} + \omega_0^2 u_{cmd} \\ m_h = K_{act}(x_{act} - \delta) \end{cases} \tag{6}$$

where $\omega_0 = 2\pi f_0$; x_{act}, $\dot{x}_{act}$ are each actuator's states, and the last equation is each actuator's output.
The physical actuators involved in wind tunnel tests are equipped with a servo-controller in the form described in [10]. To improve the reliability of numerical state-space actuator model, the simple second order system will be enriched in future by the complete servo-controller dynamics.

2.1.4 Complete ASE state-space system

By manipulating the time domain equations shown in 2, 4 and 6, it is possible to derive the complete ASE state-space model as represented in Fig. 5.

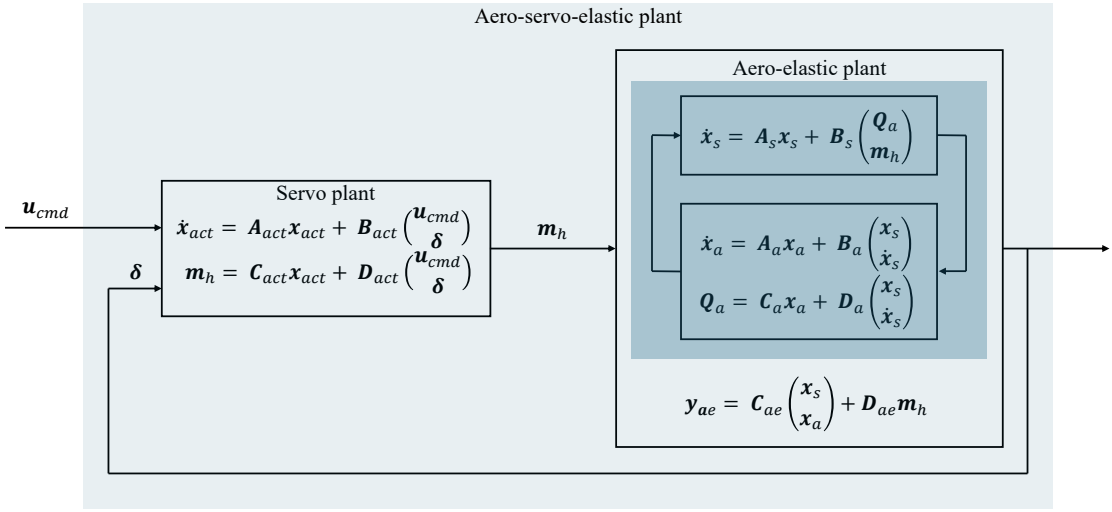


Figure 5: WTT4 ASE state-space model.

For sake of simplicity, the equations are summarized as:

$$\begin{cases} \dot{\mathbf{x}} = \mathbf{A}\mathbf{x} + \mathbf{B}\mathbf{u}_{cmd} \\ \mathbf{y} = \mathbf{C}\mathbf{x} + \mathbf{D}\mathbf{u}_{cmd} \end{cases} \tag{7}$$

with $\mathbf{x} = \{\mathbf{q}, \dot{\mathbf{q}}, \mathbf{x}_a, \mathbf{x}_{act_{ail}}, \mathbf{x}_{act_{tab}}\}$ vector of 22+22+18+2+2=66 states, $\mathbf{u}_{cmd} = \{u_{cmd_{ail}}, u_{cmd_{tab}}\}$ vector of 2 commanded rotations, $\mathbf{y}$ vector of 2 control surfaces rotations, along with the 2 velocities and accelerations, 15 accelerations of structural grid where physical accelerometers have been mounted on the experimental model, along with the 15 velocities and positions and 2 hinge moments, for a total of 53 outputs.

The state-space system has been computed for a range of wind velocities $V = [10, 55]$ [m/s] and stability has been assessed by computing $\mathbf{A}$ matrix eigenvalues. The resulting root locus is shown in Fig. 6, where it is compared with the root locus obtained by solving Eq. 1 with p-k method. Although to produce the former plot the two control surfaces have been fixed through SPC constraints, and no actuator dynamics was involved, same flutter mechanism is obtained from the two analyses, with $V_{fl} = 42$ [m/s] at $f_{fl} \simeq 3.5$ [Hz], as anticipated from V-f and V-g plots shown earlier in the document. The former plot is color-coded basing on the different

modes, while the latter represents the evolution of the states falling in the analyzed frequency range as velocity increases.

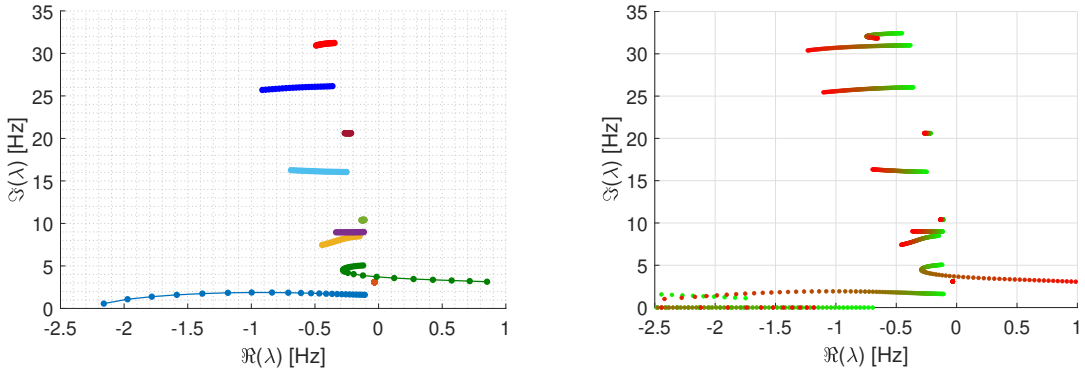


Figure 6: WTT4 root locus: p-k method (left) and state-space stability analysis (right).

The actuator dynamics does not affect flutter, and the produced state-space model can be considered a reliable representation of the FEM+DLM numerical model. The state-space form is then suitable for the design of a flutter suppression controller.

3 CONTROL STRATEGY

A two-block control strategy has been adopted in the present work. First, the AFS has been realized by means of a classical LQG with LTR corrections. Then, since the objective was to assess what happens to AFS in presence of actuation failure, the fault has been modeled by stucking one actuator. The second control block has then been introduced through an allocator capable of re-distributing the LQG/LTR control command towards the non-stuck actuator, adapting between the nominal and the faulted condition.

3.1 LQG/LTR design

An optimal LQG (LQR + LQE) has been designed on the ASE plant linearized around V_{fl}.

3.1.1 Linear Quadratic Regulator (LQR)

In the LQR approach, the optimal state-feedback gain matrix $\mathbf{K}$ is computed such that the quadratic cost functional

$$J = \int_0^\infty \left(\mathbf{x}^T\mathbf{Q}\mathbf{x} + \mathbf{u}_{cmd}^T\mathbf{R}\mathbf{u}_{cmd}\right) dt$$

is minimized. The first term penalizes the deviation of the states from the equilibrium condition, while the second penalizes the control effort. Matrices $\mathbf{Q}$ and $\mathbf{R}$ are defined so that trade-off between state regulation performance and control activity is met. In particular, since the control rationale is to suppress flutter, starting from $\mathbf{Q} = \mathbf{I}$, the diagonal terms have been updated with different values, where the highest have been assigned to the states corresponding to first and third structural modes, progressively decreasing for high frequency modes. Aerodynamics states have been kept at unitary values. For the control effort matrix $\mathbf{R}$ the same weight has been prescribed to both aileron and tab actuators. In this way, the control activity has been shaped to be more aggressive on flutter modes, yet avoiding saturation and unreasonable control surfaces activity.
With the prescribed $\mathbf{Q}$ and $\mathbf{R}$ matrices, an algebraic Riccati equation in the form

$$\mathbf{A}^T\mathbf{P} + \mathbf{P}\mathbf{A} - \mathbf{P}\mathbf{B}\mathbf{R}^{-1}\mathbf{B}^T\mathbf{P} + \mathbf{Q} = \mathbf{0}$$

is solved by determining $\mathbf{P}$. The gain matrix is finally evaluated as

$$\mathbf{K} = \mathbf{R}^{-1}\mathbf{B}^T\mathbf{P}$$

and the produced command becomes

$$\mathbf{u}_{cmd} = -\mathbf{K}\mathbf{x}.$$

Since the entire vector of states is not really available in most of real applications, a Linear Quadratic Estimator (LQE) has been introduced to estimate the states to be used by the control law.

3.1.2 Linear Quadratic Estimator (LQE)

The LQE computes the optimal observer gain matrix $\mathbf{L}$ by minimizing the effect of process and measurement noise on the state estimation error.

$$\begin{cases} \dot{\hat{\mathbf{x}}} = \mathbf{A}\hat{\mathbf{x}} + \mathbf{B}\mathbf{u}_{cmd} + \mathbf{L}(\mathbf{y}_{meas} - \hat{\mathbf{y}}) \\ \hat{\mathbf{y}} = \mathbf{C}\hat{\mathbf{x}} + \mathbf{D}\mathbf{u}_{cmd} \end{cases} \tag{8}$$

LQE equations are shown in Eq. 8, where $\hat{\mathbf{x}}$ are the estimated states, while $\mathbf{y}_{meas} - \hat{\mathbf{y}}$ represents the innovation, i.e. the difference between the measured output and its predicted value, and

$$\mathbf{y}_{meas} = \mathbf{C}_y\mathbf{x} + \mathbf{D}\mathbf{u}_{cmd}$$

are the outputs of the ASE system directly available from the sensors to be used in the wind tunnel, i.e. 15 accelerations coming from the accelerometers and 2 control surface rotations coming from the encoders mounted on the Harmonic Drive motors.
The optimal observer matrix $\mathbf{L}$ is obtained by solving an algebraic Riccati equation in the form

$$\mathbf{A}\mathbf{P} + \mathbf{P}\mathbf{A}^T - \mathbf{P}\mathbf{C}_y^T\mathbf{R}_n^{-1}\mathbf{C}_y\mathbf{P} + \mathbf{G}\mathbf{Q}_n\mathbf{G}^T = \mathbf{0}$$

and, from its solution,

$$\mathbf{L} = \mathbf{P}\mathbf{C}_y^T\mathbf{R}_n^{-1}.$$

Matrix $\mathbf{G}$ defines how process noise enters the system, i.e. which states are directly affected by model uncertainty. In this case $\mathbf{G} = \mathbf{I}$, meaning that uncertainties have been spread on all the states. The weighting matrices $\mathbf{Q}_n$ and $\mathbf{R}_n$ represent the covariance of the process and measurement noise, respectively. Since higher $\mathbf{Q}_n$ increases the observer bandwidth, a low constant value has been assigned on all the diagonal terms of the matrix, to keep the bandwidth limited. This parameter has been increased during the Loop Transfer Recovery process, explained later in the document. Matrix $\mathbf{R}_n$ reduces sensitivity to measurement noise. To account for the fact that accelerometers are generally noisier than encoders, higher values have been assigned to the diagonal terms of $\mathbf{R}_n$ correspondent to encoders measurements.

ASE closed loop system is presented in Eq. 9.

$$\begin{cases} \begin{Bmatrix} \dot{\mathbf{x}} \\ \dot{\hat{\mathbf{x}}} \end{Bmatrix} = \begin{bmatrix} \mathbf{A} & \mathbf{0} \\ \mathbf{L}\mathbf{C}_y & \mathbf{A} - \mathbf{L}\mathbf{C}_y \end{bmatrix} \begin{Bmatrix} \mathbf{x} \\ \hat{\mathbf{x}} \end{Bmatrix} + \begin{bmatrix} \mathbf{B} \\ \mathbf{B} \end{bmatrix} \mathbf{u}_{cmd} \\ \mathbf{y} = \mathbf{C}\mathbf{x} + \mathbf{D}\mathbf{u}_{cmd} \\ \mathbf{u}_{cmd} = -\mathbf{K}\hat{x} \end{cases} \tag{9}$$

3.1.3 Loop Transfer Recovery (LTR)

The estimator's presence introduces additional dynamics, partially loosing the LQR robustness. To recover it, LTR has been applied following the work of [11]. To assess the effects of LTR, disk margins are considered, as they provide a multivariable robustness measure that accounts for simultaneous gain and phase perturbations while preserving loop coupling effects [12]. Table 2 shows the results obtained on the input loop transfer function.

Table 2: Robustness recovery on LQG/LTR

Input	Gain Margin [min, max]	Phase Margin	Disk Margin
$u_{cmd_{ail}}$	$[0.19, 5.21]$	$\pm 68.3°$	1.35
$u_{cmd_{tab}}$	$[0.21, 4.59]$	$\pm 65.4°$	1.28

The schematic block diagram of the closed-loop system is presented in Fig. 7.

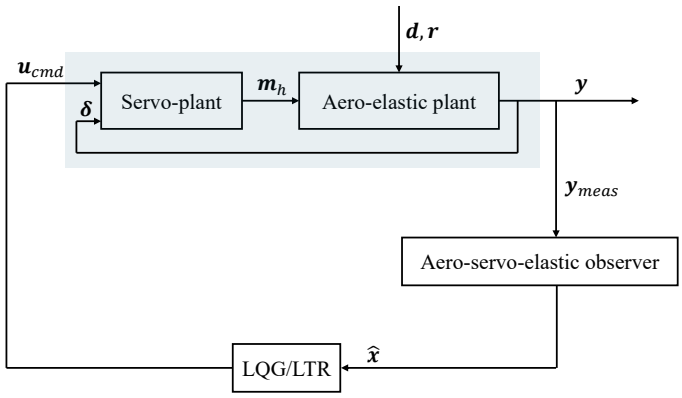


Figure 7: WTT4 ASE CL state-space model.

3.2 LQG/LTR validation

A time simulation has been computed on the open and closed-loop systems giving as input a disturbance of $2°$ on both the control surfaces and a limited bandwidth noise on the accelerometers only, in the range $f_{noise} = [0, 15]$ [Hz]. Figure 8 shows the results in terms of wing tip acceleration measure, showing the LQG/LTR ability in stabilizing the system.

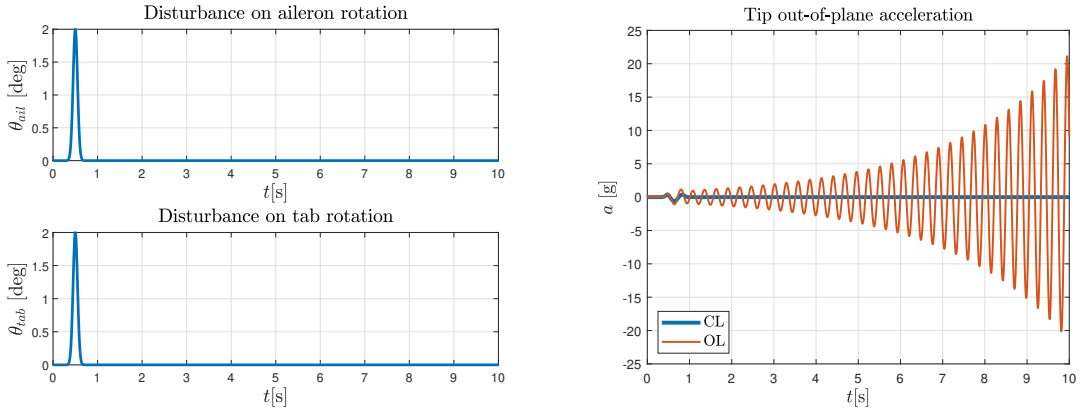


Figure 8: Time simulation: input (left) and output (right), $V = V_{fl}$.

The LQG/LTR commands are shown in Fig. 9 along with aileron and tab rotations generated by the ASE plant response to the disturbance. These two plots represent the inputs of actuator system in the form of Eq. 6.

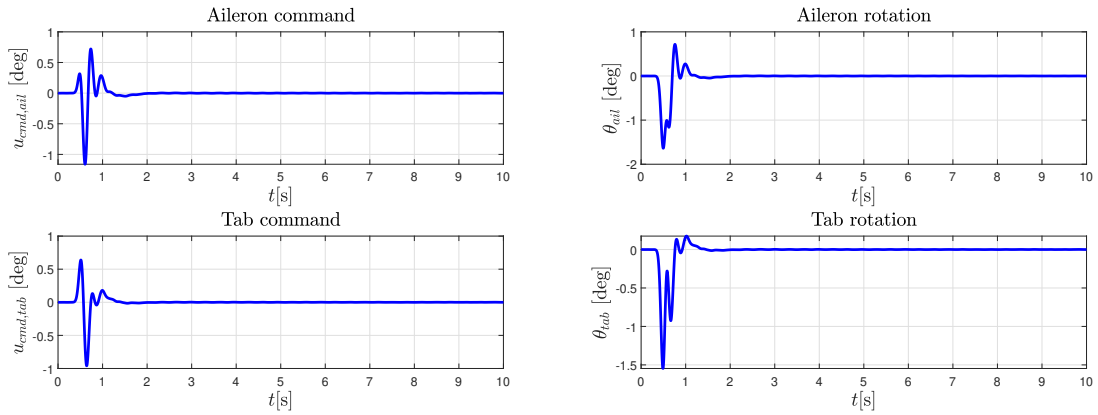


Figure 9: Actuators inputs: command (left) and actual rotation (right).

The LQG/LTR block will from now on be freezed as it is.

3.3 Actuator fault

As anticipated, the actuation failure considered in the current work is a stuck. Due to this kind of fault, the hit actuator is considered unable to respond dynamically. To model the condition, Eq. 6 have been modified by adding the following relation:

$$\begin{cases} \dot{x}_{act} = \begin{cases} \dot{x}_{act} & t < t_{\text{fault}} \\ 0 & t \geq t_{\text{fault}} \end{cases} \\ \ddot{x}_{act} = -\omega_0^2 x_{act} - 2\xi\omega_0 \dot{x}_{act} + \omega_0^2 u_{cmd} \\ m_h = K_{act}(x_{act} - \delta) \end{cases} \tag{10}$$

which leads to

$$x_{act} = \begin{cases} x_{act}(t) & t < t_{\text{fault}} \\ x_{act}(t_{fault}) = \text{constant} & t \geq t_{\text{fault}} \end{cases}$$

meaning that, starting from the time instant correspondent to the fault, the stuck actuator state does no longer evolve. Matrices $\mathbf{A}_{act}$ and $\mathbf{B}_{act}$ of Fig. 7 have been updated accordingly.

3.4 Allocator block

Even though the AFS design has involved both the control surfaces, an actuation stuck might still have some unpredictable effects on the control success. To this aim, with reference to Fig. 7, an allocation block has been introduced between the LQG/LTR and the servo-plant, receiving as input the commands produced by the AFS controller, and redistributing them on the actuators considering their actual effectiveness. The allocation law is reported in Eq. 11:

$$\begin{Bmatrix} u_{a_{ail}} \\ u_{a_{tab}} \end{Bmatrix} = \begin{bmatrix} \eta_{ail} & \alpha_{ail}(1-\eta_{tab}) \\ \alpha_{tab}(1-\eta_{ail}) & \eta_{tab} \end{bmatrix} \begin{Bmatrix} u_{cmd_{ail}} \\ u_{cmd_{tab}} \end{Bmatrix} \tag{11}$$

where η_{ail} and η_{tab} are the effectiveness of the two control surfaces, assuming value 1 in case nominal behavior is preserved, or lower values depending on the failure. When $\eta = 0$, it means that the associated actuator is stuck.
The proposed allocator keeps unchanged the AFS control action when both the actuators work in nominal conditions ($\eta_{ail} = \eta_{tab} = 1$), while transfers all the faulted actuator command towards the functioning one when stuck is experienced.
For sake of simplicity, in the current work is considered the case where the aileron gets stuck, whilst the tab maintains its nominal behavior. Hence $\eta_{ail} = 0$, $\eta_{tab} = 1$. The allocator block therefore produces:

$$\begin{Bmatrix} u_{a_{ail}} \\ u_{a_{tab}} \end{Bmatrix} = \begin{bmatrix} 0 & 0 \\ \alpha_{tab} & 1 \end{bmatrix} \begin{Bmatrix} u_{cmd_{ail}} \\ u_{cmd_{tab}} \end{Bmatrix} \tag{12}$$

meaning that the command of the tab actuator is still entirely sent to the tab, whilst the command of the aileron is also sent to the tab actuator, yet filtered by the coefficient α_{tab}, introduced to avoid saturation.
The schematic block diagram of the closed-loop system, including the allocation block, is presented in Fig. 10.

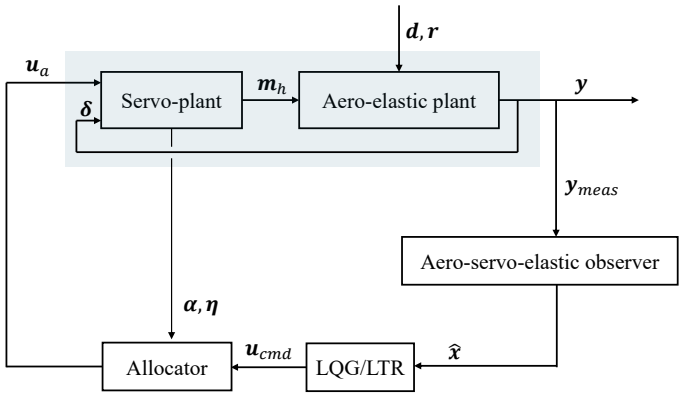


Figure 10: WTT4 ASE CL+allocator state-space model.

4 RESULTS

A time domain analysis with the same disturbance of Fig. 8 is proposed in this Section, however with the addition of aileron stuck at $t_{fault} = 0.5$ [s], i.e. when the disturbance is maximum, such that the aileron actuator state remains blocked at a non-zero value. The same analysis is applied to both the closed-loop system with just LQG/LTR block (Fig. 7), and the closed-loop system with both LQG/LTR and allocation block (Fig. 10). A value of $\alpha_{tab} = 1$ has been considered, because no saturation has been evidenced from the analyses.
Figure 11 shows the control surfaces commands given as input to the actuators, with and without allocator. Even though the aileron actuator is stuck, the LQG/LTR has no information regarding the actuators' health, therefore it still produces both the commands. However, through the coupling with the aeroelastic system, the malfunction manifests itself through persistent oscillations that were not present in the nominal case of Fig. 9. This produces a clear peak around flutter frequency in the commands' Power Spectral Density (PSD). In other words: due to the loss of one actuator, the command insists longer on flutter frequency to keep system stability.

When allocation is implemented, the aileron command goes to 0 after the stuck, and no energy is spent in producing a command that won't be used. Additionally, the tab command PSD is more homogeneous around low frequencies, and oscillations are damped in less than 2 seconds.

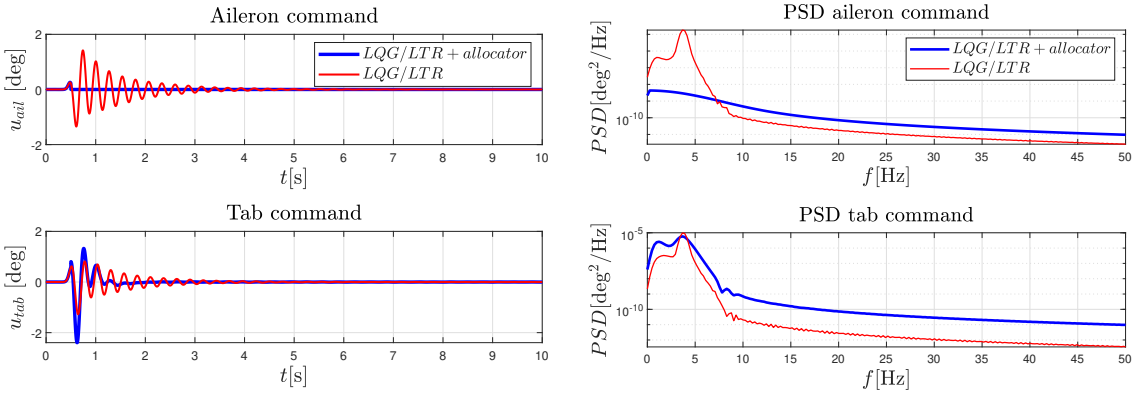


Figure 11: Allocated and non-allocated commands: time histories (left) and PSD (right).

The actual control surfaces rotations are shown in Fig. 12. For both the tested systems, the aileron rotation follows the disturbance and stops at the same value, accordingly to the same stuck mechanism. On the contrary, tab rotation is higher in peak when the allocator is involved, but decays much faster.

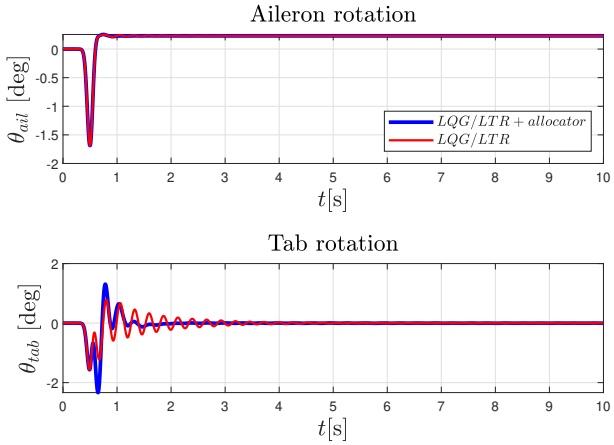


Figure 12: Control surfaces rotations with and without the allocation block.

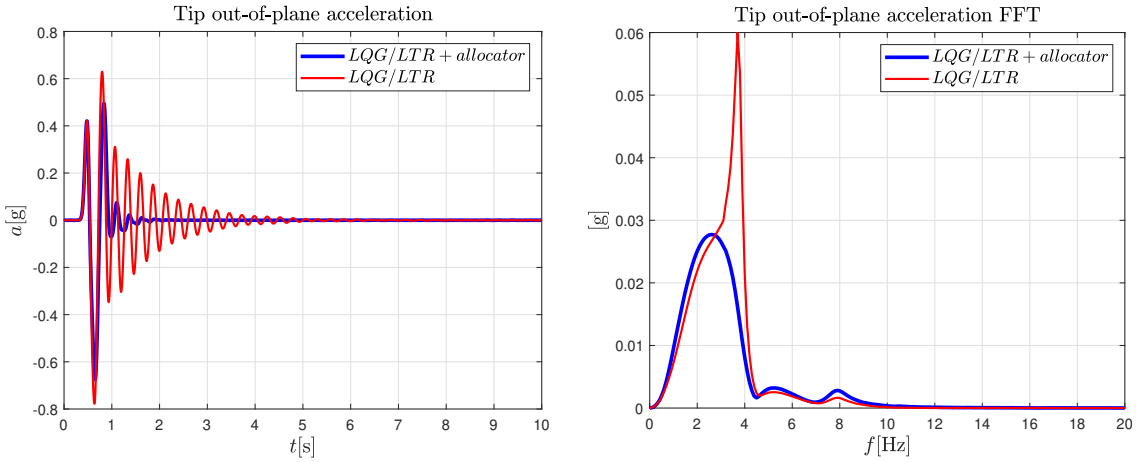


Figure 13: Wing tip acceleration with and without the allocation block: time histories (left) and Fast Fourier Transform (right).

Interestingly, as visible from Fig. 13, the allocation is not strictly necessary to guarantee stability, meaning that if the aileron actuator gets stuck, the tab alone is still capable of suppressing flutter. However, the oscillations take longer to run out, while with the allocator the time is significantly reduced to values comparable with the nominal case, i.e. without any failure. The Fast Fourier Transform (FFT) confirm this result, clearly showing how the same frequency content is present in the compared signals, yet with significantly different peak amplitude around $f = f_{fl} = 3.5$ [Hz], meaning that the presence of allocator dissipates the signal energy associated to this frequency much faster.

5 CONCLUSIONS AND FUTURE DEVELOPMENTS

A state-space model of an aero-servo-elastic system has been realized and studied in the present work. Thanks to the presence of redundant actuators, AFS based on LQG/LTR has been designed exploiting both the control surfaces and tested in case of one actuator stuck. The results have shown that one control surface is sufficient to suppress flutter. However, by implementing an allocation block that adapts to actuation faults, the command generated by the AFS can be completely exploited by the functioning control surface, minimizing time decays and command energy waste.
The results obtained seem promising and will be validated during wind tunnel test campaign on the WTT4 model for the HERA flutter suppression demonstrator.
A critical aspect to be considered in view of the experimental tests is the calculation of η. The parameter is necessary for the allocator to properly re-distribute the load, and must be evaluated starting from physical quantities that express the operating conditions of each actuator. This topic is currently under study.

6 ACKNOWLEDGEMENTS

This study is part of the Hybrid-Electric Regional Architecture (HERA) project. This project has received funding from the Clean Aviation Joint Undertaking under the European Union's Horizon Europe research and innovation programme under Grand Agreement HERA (Hybrid-Electric Regional Architecture) n° 101102007. Views and opinions expressed are however those of the authors only and do not necessarily reflect those of the European Union or the Clean Aviation Joint Undertaking. Neither the European Union nor the granting authority can be held responsible for them.

7 REFERENCES

[1] Hera: Hybrid electric regional architecture. `https://project-hera.eu/home`.

[2] Livne, E. (2018). Aircraft active flutter suppression: State of the art and technology maturation needs. *Journal of Aircraft*, 55(1), 410–452.

[3] Roncolini, E., Toffol, F., Ricci, S., et al. (2025). Impact of adopting active flutter suppression systems on the optimization of a typical long-range transport aircraft. In *AeroBest2025 III ECCOMAS Thematic Conference on Multidisciplinary Design Optimization of Aerospace Systems*. IDMEC Instituto Superior Técnico Universidade de Lisboa, pp. 387–406.

[4] Cavagna, L., Ricci, S., and Travaglini, L. (2011). NeoCASS: An Integrated Tool for Structural Sizing, Aeroelastic Analysis and MDO at Conceptual Design level. doi:10.1016/j.paerosci.2011.08.006.

[5] Cavagna, L., Ricci, S., and Riccobene, L. (2011). Structural Sizing, Aeroelastic Analysis, and Optimization in Aircraft Conceptual Design. *Journal of Aircraft*, 48, 1840–1855. ISSN 0021-8669. doi:10.2514/1.C031072.

[6] Cavagna, L., Ricci, S., and Travaglini, L. (2011). Aeroelastic Analysis and Optimization at Conceptual Design Level Using NeoCASS Suite. In *Collection of Technical Papers - AIAA/ASME/ASCE/AHS/ASC Structures, Structural Dynamics and Materials Conference*. ISSN 02734508. doi:10.2514/6.2011-2079.

[7] Marchetti, L. (2024). *Developments in aeroelastic wind tunnel testing for high aspect ratio wing configurations*. Phd thesis, Politecnico di Milano, Milan.

[8] Ricci, S., Marchetti, L., Riccobene, L., et al. (2021). An active flutter suppression (afs) project: Overview, results and lessons learned. In *AIAA Scitech 2021 Forum*. p. 0908.

[9] Ripepi, M. and Mantegazza, P. (2013). Improved matrix fraction approximation of aerodynamic transfer matrices. *AIAA journal*, 51(5), 1156–1173.

[10] De Gaspari, A. and Mantegazza, P. (2024). Dual loop pi m pi n control for an aileron positioning. *IEEE Access*, 12, 56120–56140.

[11] Doyle, J. and Stein, G. (2003). Robustness with observers. *IEEE transactions on automatic control*, 24(4), 607–611.

[12] Seiler, P., Packard, A., and Gahinet, P. (2020). An introduction to disk margins [lecture notes]. *IEEE Control Systems Magazine*, 40(5), 78–95.

COPYRIGHT STATEMENT

The authors confirm that they, and/or their company or organisation, hold copyright on all of the original material included in this paper. The authors also confirm that they have obtained permission from the copyright holder of any third-party material included in this paper to publish it as part of their paper. The authors confirm that they give permission, or have obtained permission from the copyright holder of this paper, for the publication and public distribution of this paper as part of the IFASD 2026 proceedings or as individual off-prints from the proceedings.